High-resolution coherency functionals for velocity analysis: An application for subbasalt seismic exploration

Andrea Tognarelli[1], Eusebio Stucchi[2], Alessia Ravasio[3], and Alfredo Mazzotti[1]

ABSTRACT

We tested the properties of three different coherency functionals for the velocity analysis of seismic data relative to subbasalt exploration. We evaluated the performance of the standard semblance algorithm and two high-resolution coherency functionals based on the use of analytic signals and of the covariance estimation along hyperbolic traveltime trajectories. Approximate knowledge of the wavelet was exploited to design appropriate filters that matched the primary reflections, thereby further improving the ability of the functionals to highlight the events of interest. The tests were carried out on two synthetic seismograms computed on models reproducing the geologic setting of basaltic intrusions and on common midpoint gathers from a 3D survey. Synthetic and field data had a very low signal-to-noise ratio, strong multiple contamination, and weak primary subbasalt signals. The results revealed that high-resolution coherency functionals were more suitable than semblance algorithms to detect primary signals and to distinguish them from multiples and other interfering events. This early discrimination between primaries and multiples could help to target specific signal enhancement and demultiple operations.

INTRODUCTION

Velocity analysis is carried out by measuring the coherency on trace samples selected along the hyperbolic trajectories that approximate the moveout curve. There are many methods for computing coherency: The most common is the semblance coefficient, i.e., the normalized energy ratio between the output and input traces, where the output trace is obtained by stacking the input traces (Neidell and Taner, 1971). Biondi and Kostov (1989) intro-
duce a method for computing high-resolution velocity spectra based on the eigenstructure decomposition of the covariance matrix of the data and discuss its derivation for narrow and broadband signals. In the same class of algorithms, Key et al. (1987) and Key and Smithson (1990) propose a coherency measure that applied to the computation of velocity spectra resolves reflections closely spaced in time and moveout. Jones and Levy (1987) demonstrate the usefulness of eigenvector analysis of the data covariance matrix also for other applications such as the separation of the signal from various kinds of coherent and incoherent noise.

Sacchi (1998) introduces the bootstrapping method for improving velocity estimates derived from Key and Smithson's (1990) coherency measures. In the same path, Abbad et al. (2009) propose the bootstrapped differential semblance coherency estimator to improve the resolution of nonhyperbolic moveout parameters and to develop an automatic velocity analysis. They also discuss its applicability to estimate relevant anisotropy parameters. In another paper, Abbad and Ursin (2012) illustrate several high-resolution coherency estimators based on the bootstrapping process at a comparable computational cost to a standard semblance estimator.

Another type of coherency estimator makes use of the a priori knowledge of the seismic wavelet. Spagnolini et al. (1993) suggest exploiting a priori knowledge of the wavelet amplitude spectrum for the coherency measure and then propose complex matched filter analysis. As Grion et al. (1998) show on synthetic and field data, an approximate knowledge of the wavelet is sufficient to exploit the ability of the complex matched functional to reject random and coherent noise and to improve the resolution of the velocity estimates. In other works (Grandi et al., 2004, 2007), the advantages of the method based on data covariance and of the method based on matched filtering are jointly exploited by evaluating the eigensolutions of the covariance matrix of the data convolved with a complex matched filter.

In general, the need for high-resolution tools for velocity analyses increases when the interference of primaries, multiples, and

converted waves makes it difficult to extricate the useful (low-amplitude) signal from various kinds of noise. The seismic data acquired for the exploration of subbasalt targets represent typical cases. The peculiar high reflectivity and high attenuation of the thick basaltic layers limit the downward propagation of the seismic pulses and generate sets of multiple reflections at a high amplitude. Also, the often extremely heterogeneous basalts produce high-frequency scattering of the seismic energy, thus further decreasing the signal-to-noise ratio (S/N) (Ziolkowski et al., 2003).

Various innovative seismic methods have been proposed to improve subbasalt imaging. Some refer to seismic acquisition technology, while others focus on S/N increase by specific processing sequences. Fliedner and White (2001), Fruehn et al. (2001), and White et al. (2003) exploit the traveltimes and amplitudes of the diving waves recorded at very long source to receiver offsets (up to 38 km) to derive reliable estimates of the seismic velocity and thickness of the basalt layers; they then integrate this information in the prestack depth migration of reflections at various offset ranges. Ziolkowski et al. (2003) suggest that acquisition techniques should be tailored to enhance the low frequencies of the spectrum where the subbasalt signal is more likely to be found. Thus, they propose using large air gun arrays with increased total volume and deep towing of the source and the streamer. Similarly, Woodburn et al. (2011) stress the importance of low frequencies for subbasalt imaging and discuss the application of a low-frequency boosting filter at the start of the processing. Also, the use of broadband seismic acquisition techniques, able to extend the data bandwidth on high and low frequencies, has recently been suggested (Spjuth et al., 2012) as has the use of processing solutions to achieve the same objective (e.g. Zhou et al., 2012).

Gallagher and Dromgoole (2008) perform a comprehensive study of various kinds of marine seismic data, acquired with different sources, streamer lengths, and source and streamer depths. They conclude that fine-tuning of the acquisition is indeed beneficial, but a processing sequence, focused on the low frequencies of the spectrum and on accurate multiple removal and velocity analysis, is crucial.

Despite such advances in acquisition and processing, the imaging below basalt layers still remains a challenge for seismic exploration. Our aim is to improve the identification of the stacking velocity of the weak subbasalt signals at an early stage of the processing. In fact, Gallagher and Dromgoole (2008) underline the importance and the difficulty of knowing the velocity model: They showed that even with good multiple suppression techniques, the velocity analysis can be difficult to interpret. Indeed, multiple removal is a thorny issue because demultiple operations, which are often performed repeatedly, can also lead to the loss of the weak subbasalt primaries. It is therefore important to be able to detect the weak signals and to discriminate between them and the high-amplitude multiples as early as possible in the processing sequence. Using synthetic and field data, we thus tested different coherency functionals for the velocity analysis of subbasalt seismic data and assessed their performance in terms of signal and coherent noise discrimination.

HIGH-RESOLUTION COHERENCY FUNCTIONALS

Coherency measures provide quantitative information regarding the degree of correlation between signals among data traces. One of their main applications in seismic data processing is stacking velocity analysis. Various implementations are available that differ in terms of their resolution capability and their ability to discriminate between signals and random and nonrandom noise.

The most commonly used is the semblance functional C_s (Neidell and Taner, 1971), which, when computed on a time window centered along the hyperbolic trajectory defined by t_0, V_{stack}, can be written as

$$C_s = \frac{1}{M} \frac{\sum_{t=t_0-T/2}^{t=t_0+T/2} \left(\sum_{i=1}^{M} d_i(t_0; V_{stack}) \right)^2}{\sum_{t=t_0-T/2}^{t=t_0+T/2} \sum_{i=1}^{M} d_i^2(t_0; V_{stack})}, \qquad (1)$$

where i is the index of the M traces (i.e., the columns) of a seismic data gather d and T is the width of the time window.

Semblance yields an accurate, low-resolution, coherency estimation under the assumption of a zero-mean uncorrelated noise. If nonrandom noise contaminates the data, the semblance measure is biased. As shown later, the low-resolution characteristics and the sensitivity to coherent noise make it difficult for the semblance to discern weak subbasalt signals interfered with strong multiple reflections and by converted waves.

Sguazzero and Vesnaver (1987) introduce complex-valued coherency functionals operating on complex-valued traces, which emphasize phase correlation among traces and can reduce the estimate uncertainty. They demonstrate that even simple normalized correlation using complex signals can improve resolution. On this basis, Spagnolini et al. (1993) suggest using the (approximate) knowledge of the a priori wavelet to filter the data before evaluating the coherency along the hyperbolic trajectory.

We thus define the complex matched semblance (C_{cm}) making use of the analytic signals of the seismic data gather d and of the wavelet, computed via the Hilbert transform. Therefore, for a time window centered along the hyperbolic trajectory (t_0, V_{stack}), the C_{cm} estimate is expressed as

$$C_{cm} = \frac{1}{M} \frac{\sum_{t=t_0-T/2}^{t=t_0+T/2} \left| \sum_{i=1}^{M} (D_i; t_0, V_{stack}) \right|^2}{\sum_{t=t_0-T/2}^{t=t_0+T/2} \sum_{i=1}^{M} |(D_i; t_0, V_{stack})|^2}, \qquad (2)$$

where D_i is the analytic data filtered by the analytic wavelet.

As Grion et al. (1998) show, these types of functionals are quite robust because the use of complex signals does not require constraints on the wavelet phase: even when using approximate wavelets, with amplitude spectra roughly matching the field data spectrum, they give a satisfactory S/N discrimination.

Using the eigenvalue analysis of the data covariance matrix, Key and Smithson (1990) separate the contribution of the signal from that of the noise. Assuming that noise and signal are uncorrelated with zero mean and variances σ_N^2 and σ_S^2, and that noise is uncorrelated among traces, the S/N within a time window centered along a hyperbolic trajectory can be expressed as

$$S/N = \frac{\lambda_1 - \sum_{i=2}^{M} \frac{\lambda_i}{(M-1)}}{\sum_{i=2}^{M} \frac{\lambda_i}{(M-1)}}, \qquad (3)$$

where M is the number of traces and λ_i are the eigenvalues computed on the data covariance matrix $d^T d$, sorted in decreasing order (the superscript T means the transpose operator).

If a signal is present along the sought-after trajectory, then $\lambda_1 = \sigma_S^2 + \sigma_N^2$ and $\lambda_i = \sigma_N^2$ for $2 \leq i \leq M$. The noise variance is obtained by averaging the $2 \leq i \leq M$ eigenvalues as

$$\sigma_N^2 = \sum_{i=2}^{M} \frac{\lambda_i}{(M-1)}. \tag{4}$$

Weighting the Key and Smithson (1990) S/N estimate of equation 3 by the complex matched functional of equation 2, we obtain the following coherency functional:

$$C_{\mathrm{cmKS}} = \mathrm{S/N}\, C_{\mathrm{cm}}. \tag{5}$$

The combined use of a complex matched filter based on a priori knowledge of the wavelet and of the coherency measure by the eigenstructure analysis of the data covariance matrix, as suggested by Grandi et al. (2004 and 2007) and expressed by the coherency functional in equation 5, resolves closely spaced events in time and in velocity. Furthermore, if crossing events occur, such as multiples or converted waves that intersect primaries, they do not contribute to the signal estimation, but only increase the noise variance. This results in a lower S/N estimate without compromising the resolution. We call this new coherency estimator C_{cmKS}, i.e., complex matched plus Key and Smithson.

In the following sections, we discuss the capability of each of the three coherency functionals, semblance C_s, complex matched coherence C_{cm}, and Key and Smithson on complex matched filtered data C_{cmKS}, to detect and resolve weak primary subbasalt events interfered by strong multiples and buried in noise.

APPLICATION TO SYNTHETIC DATA

We considered two different 1D depth models (Figure 1) taken from Fruehn et al. (2001) and Spitzer et al. (2003). We modified them to create different patterns of interference between primaries and multiples.

Model 1 consists of six interfaces separating a top water layer of 1125 m, a sedimentary layer of 1500 m, a thick (about 600-m) basaltic bed, followed by three sedimentary strata, for a total model depth of about 4500 m. This model is designed to cause an overlap at a near-zero offset of the top basalt reflection with the first sea bottom multiple at about 3 s (Figure 2a). This is a feature of the field data examples that follow. The P- and S-wave velocities as well as the densities of the rock strata and the attenuation coefficients (α) for P-waves are taken from the cited references. Note the high attenuation of the basalt layer.

Unlike model 1, model 2 (Figure 1b) has an additional interface within the sedimentary layer overlying the basalt. The significant impedance contrast that characterizes this interface causes additional peg-leg multiples, which intersect the primary subbasalt reflections. However, the new velocity structure above the basalt layer causes the top basalt reflection to be shifted at lower two-way times, losing its simultaneous occurrence with the first sea-bottom multiple as observed in the previous model (Figure 2b).

Synthetic CMP seismograms are generated on these two models using the reflectivity method, thus enabling all the reflection, transmission, conversion, attenuation and reverberation effects to be computed. The simulated parameters are: 6-m source depth, 8-m receiver depth, 81 traces spaced 50 m, 225-m minimum offset. Both seismograms are generated using a 20-Hz central frequency wavelet and a 2-ms sample rate.

The resulting noise-free synthetic seismograms are shown in Figure 2 and in the close-ups in Figure 3a. Note the very low amplitudes of the reflections below the top basalt event, including the base basalt reflection, compared with the multiples and the converted waves.

To simulate the low S/N observed in many field data cases, we add Gaussian random noise to the synthetic data, thus obtaining the seismograms shown in Figure 3b. Only the top basalt reflections remain clearly visible, whereas the primary events below are ob-
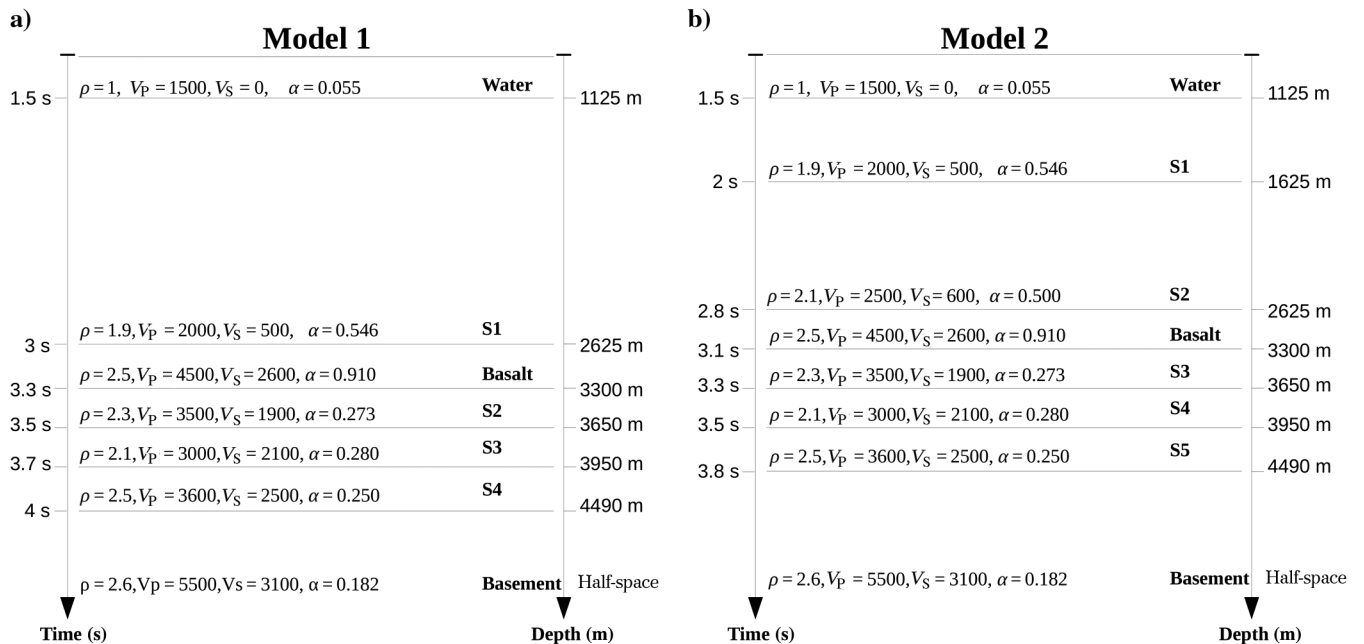

Figure 1. Depth models used to compute the synthetic common midpoint (CMP) gathers used in this study: (a) Model 1 and (b) model 2. Velocities are in m/s, densities are in g/cm³, and the attenuation coefficients are in dB/λ.

scured by the noise and only the multiples can be easily tracked. It is on these two noise-contaminated seismograms that we evaluate the performance of the velocity analysis functionals introduced in the section "High-Resolution Coherency Functionals". In both of these examples, the wavelet we used as the matching filter is a Ricker wavelet with central frequency of 15 Hz. The width of the time win-

dow for velocity analysis is 128 ms, which approximately corresponds to the length of the wavelet.

The results for the seismogram of model 1 are shown in Figure 4. Figure 4a shows the velocity analysis panel obtained via the application of the standard semblance coherency functional C_s. The outcomes of the application of the complex matched coherency

Figure 2. Synthetic CMP gathers computed by reflectivity modeling on the models of Figure 1: (a) model 1 CMP gather and (b) model 2 CMP gather. The arrows point to relevant primary and multiple reflections. The labels are as follows: WB, water-bottom reflection; S1, reflection from the base of the S1 layer; TB, top basalt reflection; B, basement reflection; WBM1, first water-bottom multiple; TBM1, first top basalt multiple; and S1M1, first multiple of the S1 reflection. Note that in the model 1 CMP, the top basalt reflection and first water-bottom multiple occur simultaneously. Instead, model 2 CMP shows many multiples intersecting the subbasalt reflections.
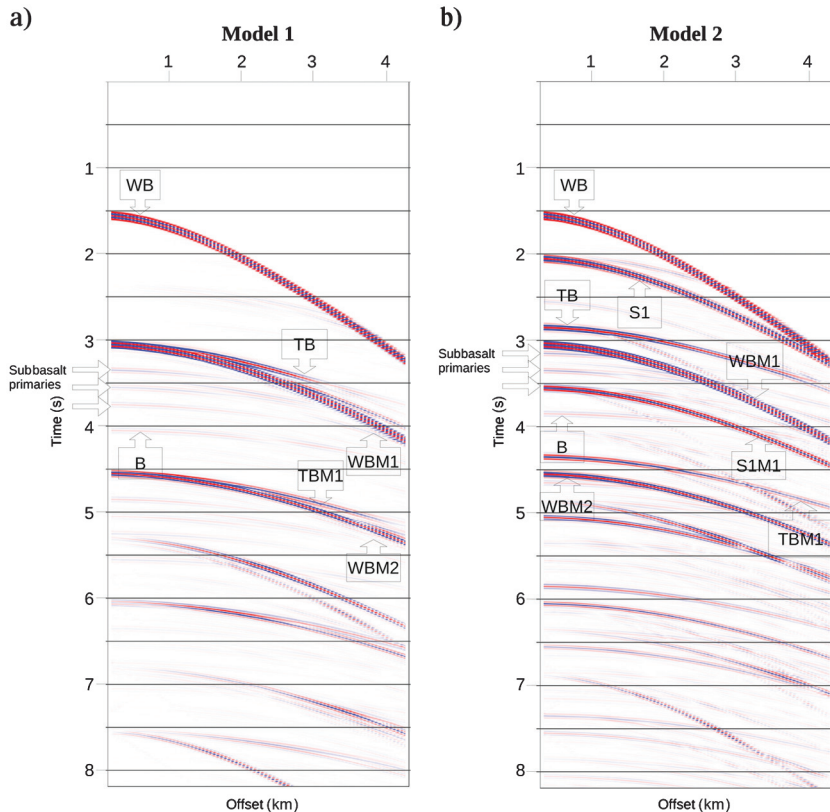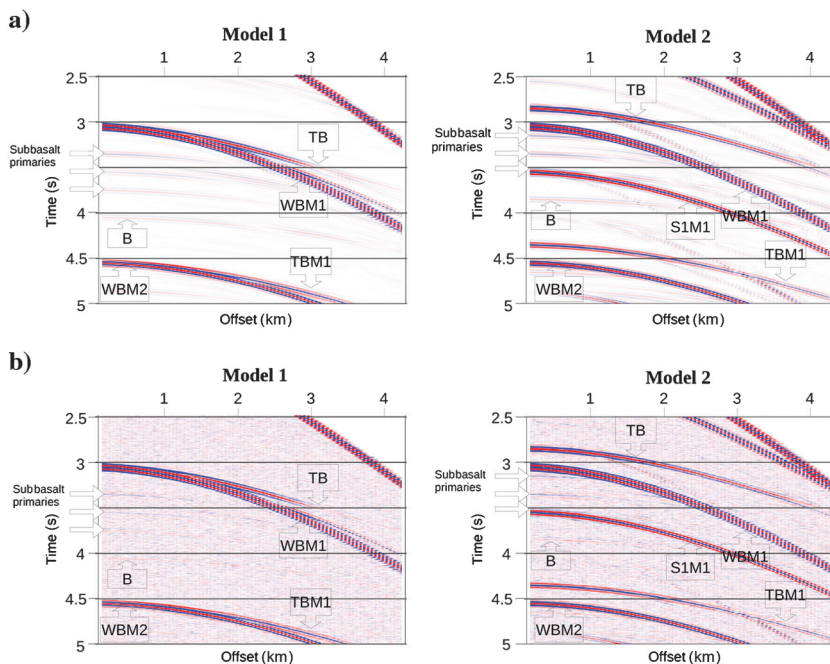

Figure 3. (a) Close-ups of the noise-free synthetic CMPs of Figure 2 (left, model 1 CMP; right, model 2 CMP). (b) Same as in (a) with added Gaussian noise. The close-ups highlight the interplay of primaries and multiples and the masking effect of noise in the time window of interest.

functional C_{cm} and the complex matched plus Key and Smithson functional C_{cmKS} are illustrated in Figure 4b and 4c, respectively. The velocity increment for velocity analysis is 20 m/s. To allow for a direct correlation of the coherency maxima with the actual reflections, Figure 4d shows the noisy synthetic data input to the velocity analysis. The velocity trend associated with the primary reflections is more evident on the C_{cm} and C_{cmKS} panels than on the semblance C_s panel, where it is barely discernible. The resolution is quite increased particularly in the C_{cmKS} panel, where the coherency maxima are well defined in time and velocity. This allows for better discrimination of the top basalt reflection from the sea-bottom multiple that occurs simultaneously at around 3 s, and for correctly picking their respective stacking velocities. Also, the stacking velocity picking of the subbasalt reflections is easily accomplished on the C_{cm} and C_{cmKS} panels. Table 1 highlights the good match between the theoretical t_0 and rms velocities and the picked values. This matching could be further improved by iterative procedures such as those that Abbad et al. (2009) outline. A proof of the increased resolution from C_s to C_{cm} to C_{cmKS} is shown in Figure 5, where the normalized coherency values are plotted as a function of the stacking velocity of the three functionals. The curves refer to five different times centered around the peaks at 3.75 s in Figure 4. The narrowest and sharpest peaks are those shown by the blue curves pertaining to the C_{cmKS} functional, followed by the red curves of the C_{cm}, and finally by the green curves of the C_s func-

tional. Therefore, the C_{cmKS} functional provides the highest resolution.

The same velocity analyses were performed on the seismogram of model 2, and the results are reported in Figure 6. In this case, there is the additional problem of the presence of multiples crossing the subbasalt reflections. However, the high-resolution coherency functionals (Figure 6b and 6c) highlight the different velocity trends better than the semblance (Figure 6a) and show the coherency maxima relative to primary events at times from 3 to 3.8 s, where

Table 1. Comparison between the theoretical t_0 and rms velocities of model 1 (shown in Figure 1a) and the t_0 and stacking velocities picked on the high-resolution (C_{cmKS}) velocity panel of Figure 4c.

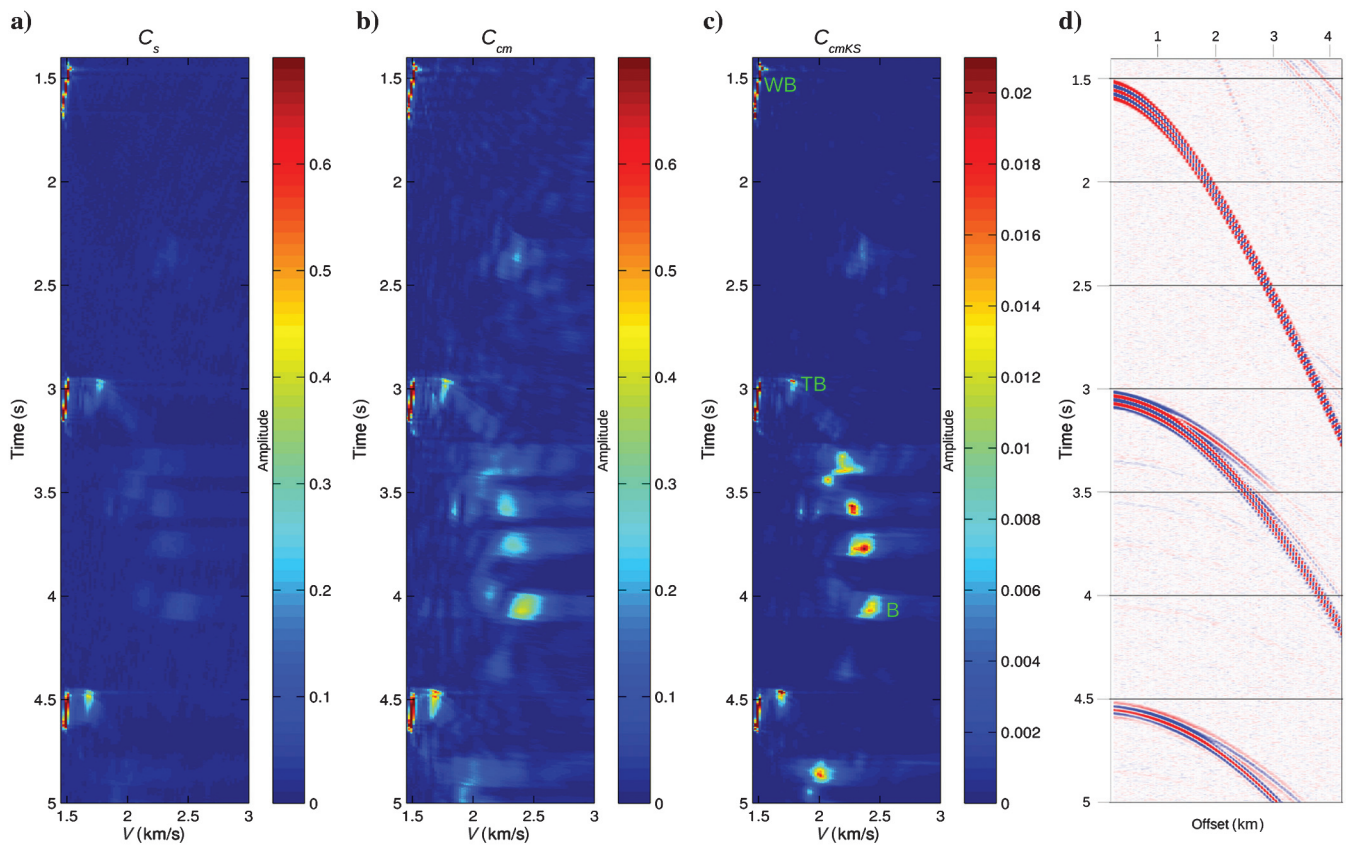| Model t_0 (s)	Picked t_0	Model V_{rms} (m/s)	Picked V_{stack}
1.5	1.5	1500	1500
3.0	3.0	1768	1790
3.3	3.39	2164	2190
3.5	3.56	2261	2270
3.7	3.77	2307	2370
4.0	4.0	2428	2410

Figure 4. Velocity spectra computed with (a) semblance (C_s), (b) complex matched coherency (C_{cm}), and (c) complex matched plus Key and Smithson (C_{cmKS}) functionals. (d) The synthetic data (model 1 CMP) input to the velocity analyses. Note that because of the high dynamic range of the C_{cmKS} functional, the corresponding velocity spectrum is plotted with a different scale in this figure and in Figure 6. The water bottom (WB), top basalt (TB), and basement (B) events are indicated in (c).
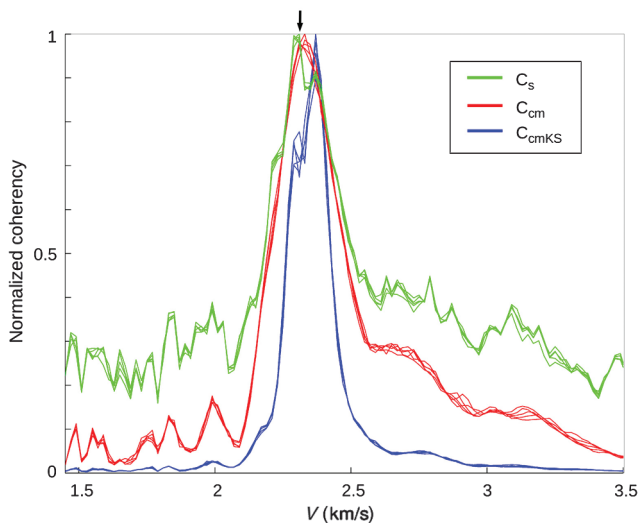
Figure 5. The normalized coherency values as a function of the stacking velocity of the C_s (green curves), C_{cm} (red curves), and C_{cmKS} (blue curves) functionals. The curves refer to five different times centered around the peaks at 3.75 s in Figure 4. The arrow indicates the true V_{rms} value of 2.3 km/s. Note that the C_{cmKS} functional has the highest resolution followed by C_{cm} and C_s.

peg-leg multiples also occur (see the input synthetic seismogram in Figure 6d for a direct correlation). Two out of four subbasalt reflections are clearly highlighted in the C_{cm} and C_{cmKS} panels in Figure 6b and 6c at 3.3 and 3.8 s. Again, the C_{cmKS} functional provides the highest resolution. As in the experiment on model 1, the picking of stacking velocities on the high-resolution coherency panels is easier than the picking on the semblance panel and leads to $t_0 - V_{stack}$ values that nicely match the model t_0 and rms velocities (Table 2). Accurate knowledge of the t_0-V_{stack} pairs could be extremely useful for subsequent operations aimed at enhancing the primaries and at removing multiples, such as the parabolic Radon demultiple, and for geometrical spreading compensation.

An additional capability of the high-resolution coherency functionals that models 1 and 2 seismograms do not allow us to test is their ability to distinguish events closely overlapping along the whole range of offsets. In those cases, whereas the semblance yields coalescing peaks or a single broad peak, the C_{cm} and (particularly) the C_{cmKS} estimators are able to produce separate peaks with greater resolution and accuracy.

APPLICATION TO FIELD DATA

We now outline the results of the application of the three coherency functionals to three different CMP gathers taken from a 3D
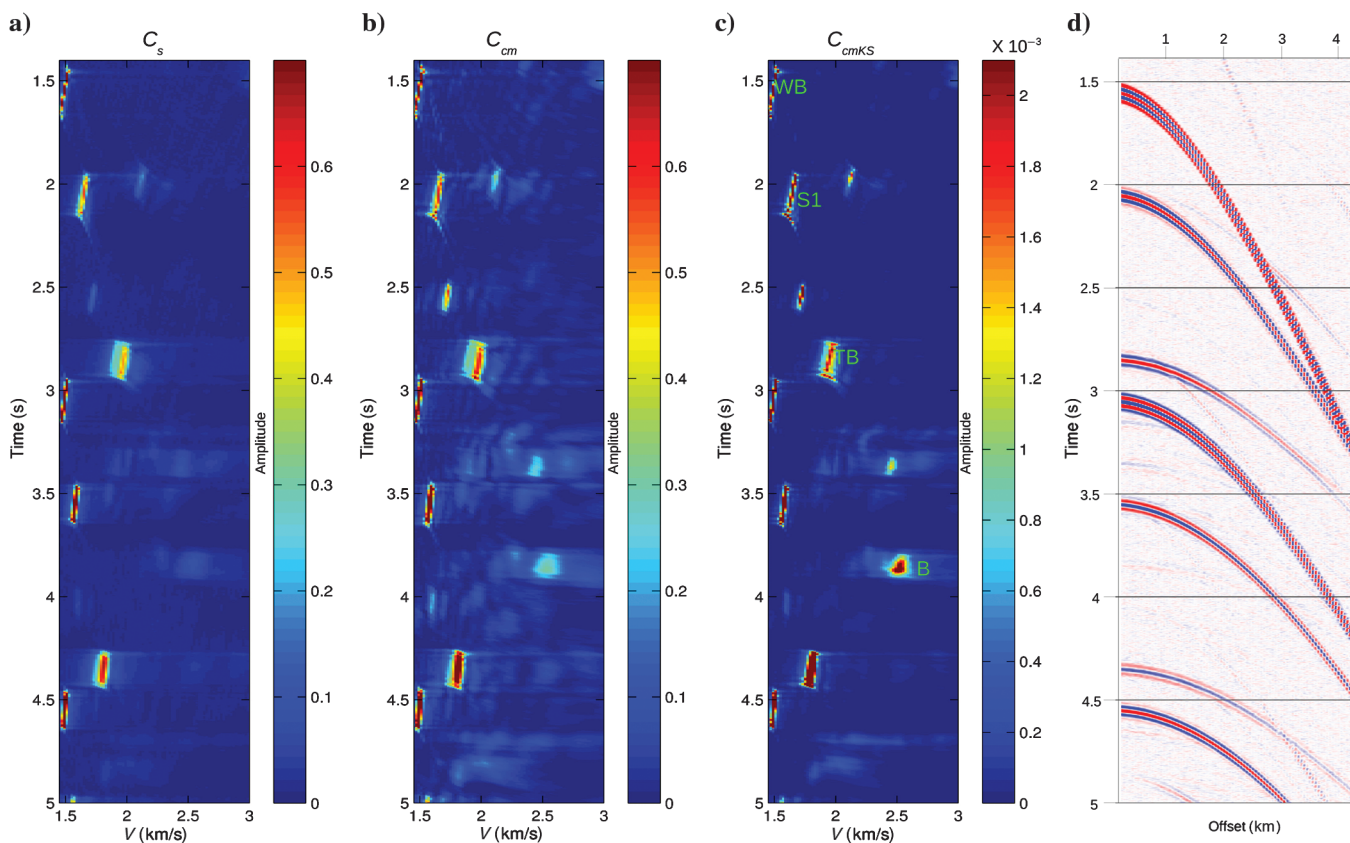

Figure 6. Velocity spectra computed with (a) semblance (C_s), (b) complex matched coherency (C_{cm}), and (c) complex matched plus Key and Smithson (C_{cmKS}) functionals. (d) The synthetic data (model 2 CMP) input to the velocity analyses. The main events and the additional S1 reflection are indicated in (c).
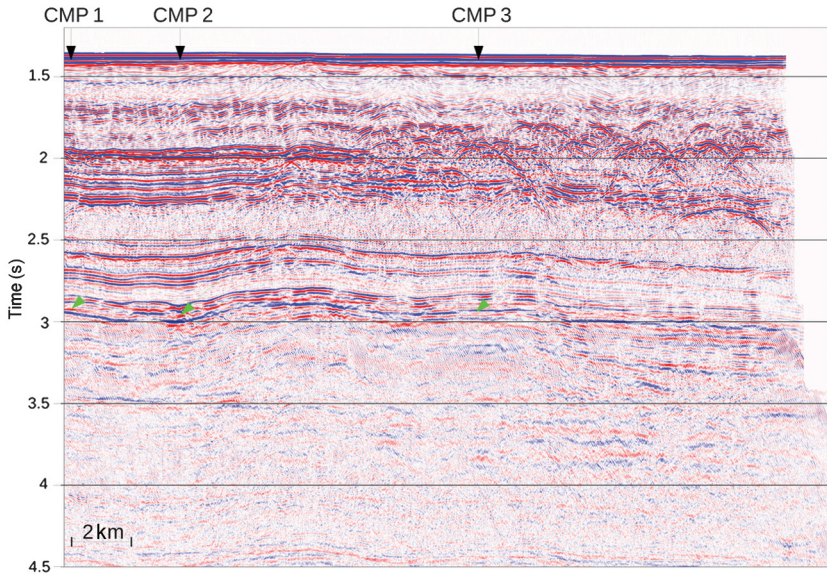
Figure 7. Raw stack section extracted along an inline of the 3D survey. The location of the three CMP gathers used for velocity analysis is indicated. The green arrows indicate the top basalt horizon.
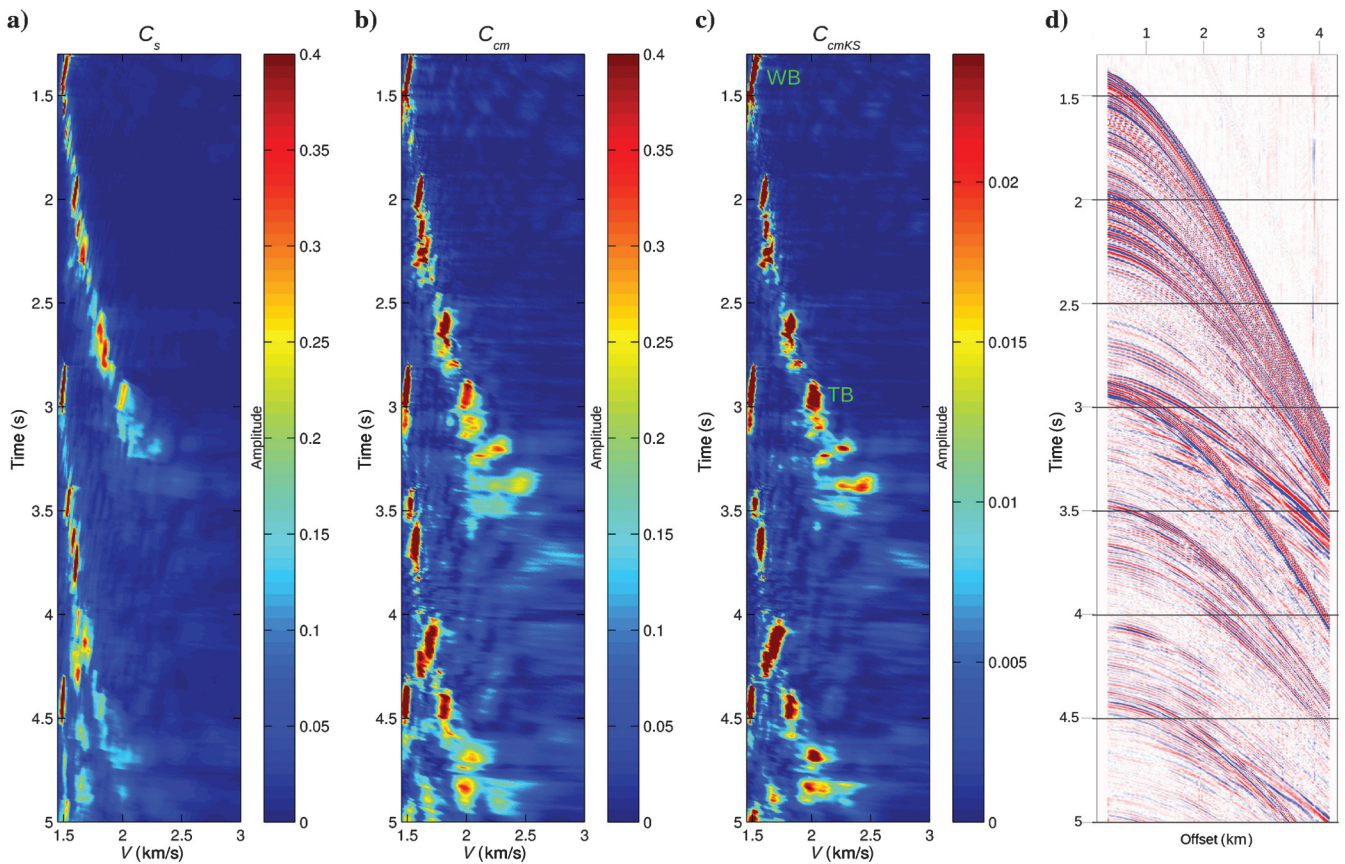

Figure 8. Velocity spectra computed with (a) semblance (C_s), (b) complex matched coherency (C_{cm}), and (c) complex matched plus Key and Smithson (C_{cmKS}) functionals. (d) The CMP gather (CMP 1 in the stack section of Figure 7) input to the velocity analyses. Note that because of the high dynamic range of the C_{cmKS} functional, the corresponding velocity spectrum is plotted with a different scale in this figure and in Figure 9. The water-bottom (WB) and the top basalt (TB) reflections are indicated in (c) both here and in Figures 9 and 10.

survey acquired in an offshore area where extensive basaltic intrusions occur within a thick sedimentary basin. The data pertain to an inline that investigates structured layers below a nearly flat sea bottom. For only the purpose of locating the test CMP gathers, Figure 7 shows the raw stack of the data after the application of high-cut filtering (0-0-90-110–110 Hz) and simple gain correction (automatic gain control, window length 500 ms). No other denoising or demultiple or signal-enhancement steps were applied.

Table 2. Comparison between the theoretical t_0 and rms velocities of model 2 (shown in Figure 1b) and the t_0 and stacking velocities picked on the high-resolution (C_{cmKS}) velocity panel of Figure 6c.

Model t_0 (s)	Picked t_0	Model V_{rms} (m/s)	Picked V_{stack}
1.5	1.5	1500	1500
2.0	2.0	1639	1650
2.8	2.8	1925	1950
3.1	Not picked	2303	Not picked
3.3	3.37	2393	2450
3.5	Not picked	2432	Not picked
3.8	3.86	2544	2530

The acquisition was carried out using air guns and multiple towed streamers, with nominal minimum and maximum source to receiver offset of 200 and 4325 m, respectively.

The CMPs in Figures 8d and 9d correspond to the locations labeled CMP 1 and CMP 2 in the stack section in Figure 7. They show many events between the sea bottom (at about 1.4 s) and the top basalt reflections (around 2.870 s). Note that, as in model 1, for both CMPs, the t_0 of the top basalt reflection nearly coincides with the t_0 of the first water-bottom multiple. Below the top basalt, some weak and discontinuous primary signals, mainly distinguishable due to their limited moveout, seem to be present but are intersected by several other events, mostly peg-leg multiples, with a higher moveout. Removing these interfering multiples while preserving the useful signal is often challenging.

Figures 8a–8c and 9a–9c show the velocity panels computed for the two CMPs by means of the different coherency functionals C_s, C_{cm} and C_{cmKS}. The velocity increment used for velocity analysis is 10 m/s. Primaries down to the top basalt reflection (at 2.8 s) and multiples below that same interface are clearly evident in all the velocity panels. However, the high-resolution velocity panels (Figures 8b, 8c, 9b, and 9c) highlight additional peaks in the spectra at times below the top basalt reflection and at velocities between 2000 m/s and 2700 m/s. These additional peaks, likely due to primaries, are not easily identifiable in the C_s panels (Figures 8a and 9a).

Similar conclusions can be drawn by examining the results obtained for the third example (Figure 10). In this case, the CMP
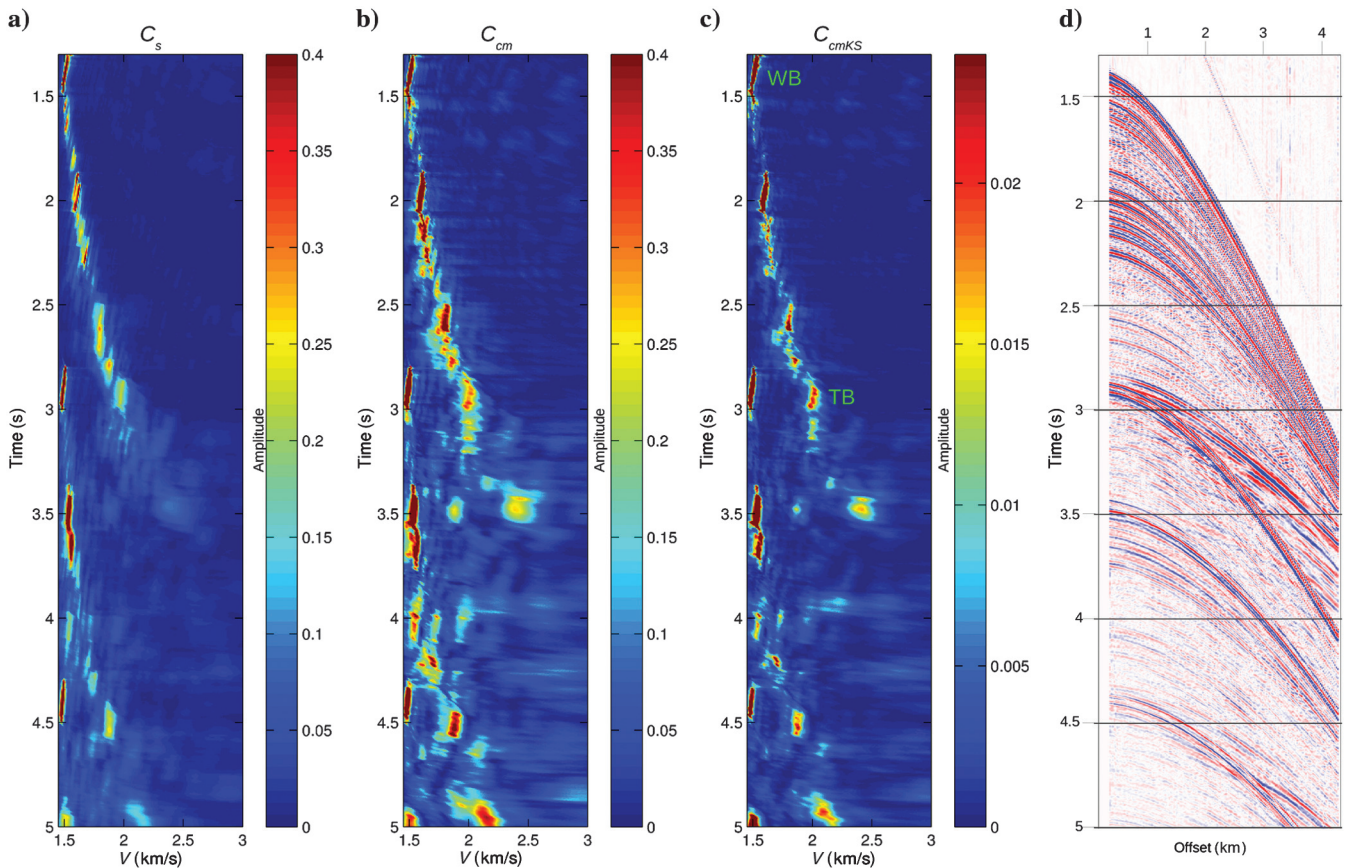

Figure 9. Velocity spectra computed with (a) semblance (C_s), (b) complex matched coherency (C_{cm}), and (c) complex matched plus Key and Smithson (C_{cmKS}) functionals. (d) The CMP gather (CMP 2 in the stack section of Figure 7) input to the velocity analyses.
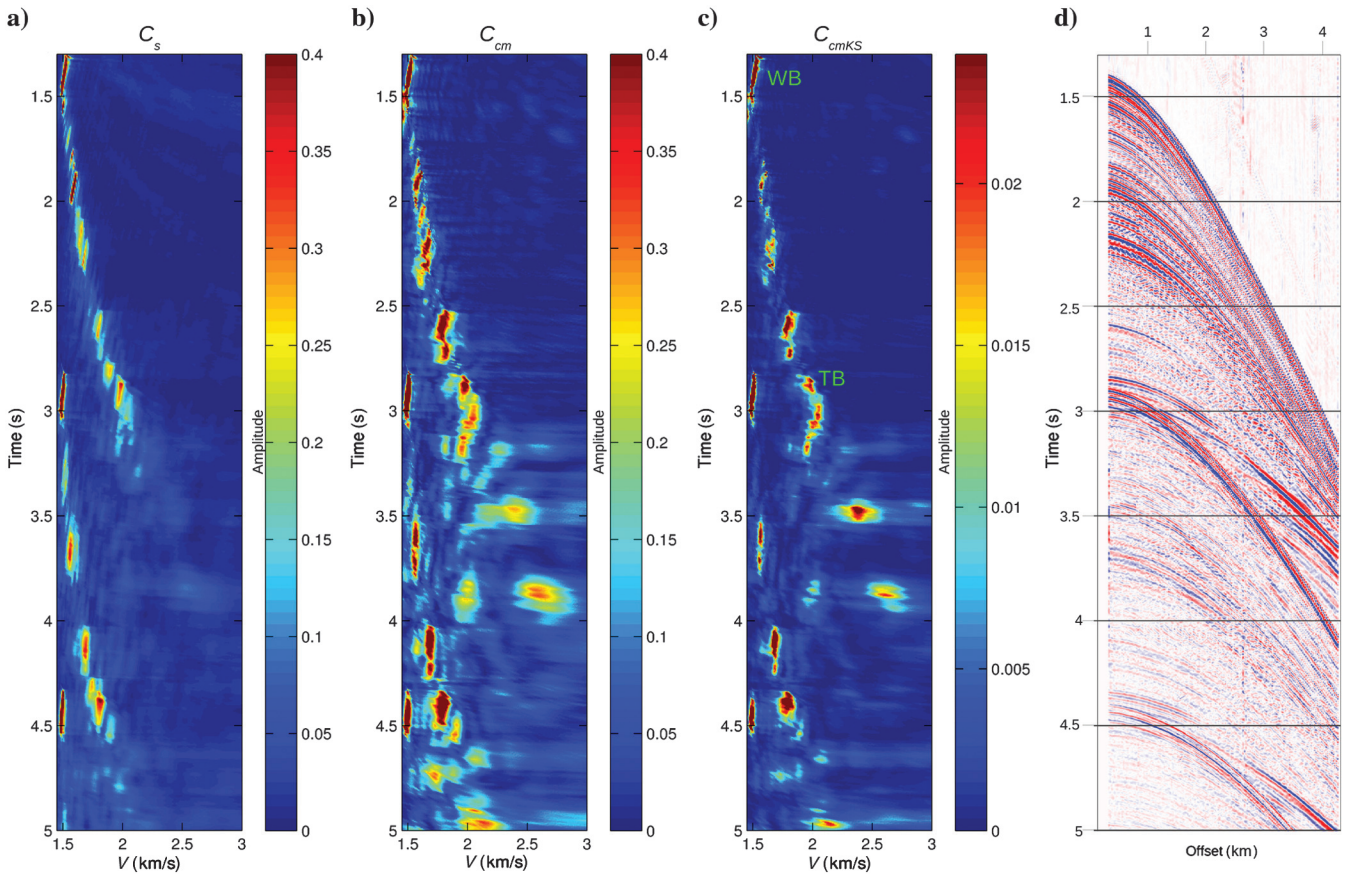
Figure 10. Velocity spectra computed with (a) semblance (C_s), (b) complex matched coherency (C_{cm}), and (c) complex matched plus Key and Smithson (C_{cmKS}) functionals. (d) The CMP gather (CMP 3 in the stack section of Figure 7) input to the velocity analyses. Note the particularly well-resolved peak at 3.9 s and 2.6 km/s, likely due to a subbasalt primary, on the C_{cmKS} panel.
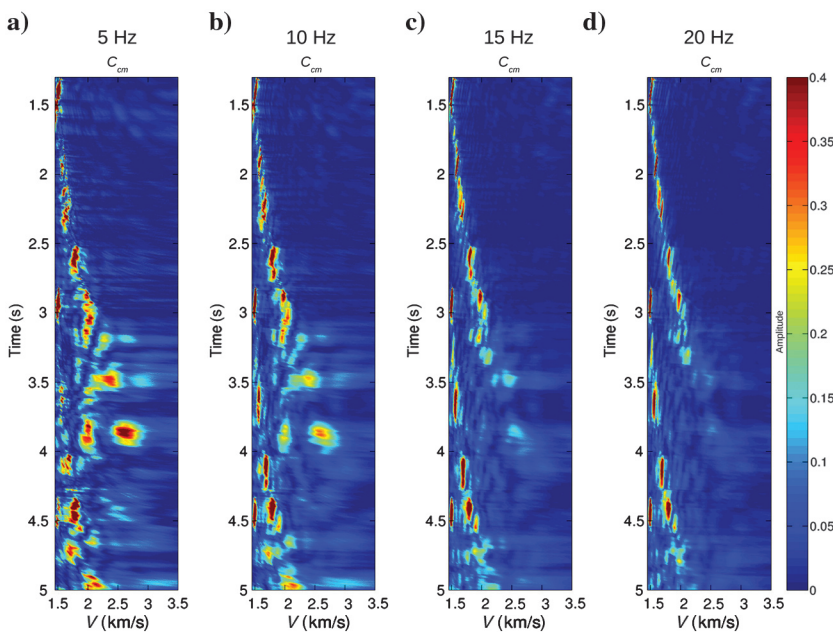

Figure 11. Comparison between the velocity spectra computed for CMP 3 with the complex matched coherency (C_{cm}) functional, using four different matching wavelets with central frequency of (a) 5, (b) 10, (c) 15, and (d) 20 Hz. Note that the subbasalt events are better resolved by the lower-frequency wavelets.

gather (Figure 10d) pertains to a location in the survey area with a more complex structural setting in the shallow part of the section (Figure 7, CMP 3 roughly between 1.8 and 2 s). However, most of the comments made for the previous examples also apply to this case: Below the top basalt reflection, it is difficult to discern primary events because there is a lot of interference. The semblance velocity panel (Figure 10a) in the critical time range from the top basalt reflection at around 2.8 s to the end of the recording is dominated by various orders of multiples. Also in this case, the high-resolution coherency functionals, and particularly the C_{cmKS} functional, are better at identifying the primary signals within this critical time window.

In all these cases, the wavelet we used as a matching filter was a Ricker wavelet with a central frequency of 10 Hz and the width of the time window for velocity analysis was 128 ms.

An additional capability of the high-resolution coherency functionals is the possibility to modify the bandwidth of the matching wavelet to chase the sought-after primary signals. In our case, the frequency band in the time windows below the top basalt reflections, including primaries and multiples and noise, reaches up to 90 Hz at −20 dB. However, it is known that for subbasalt reflections, primary signals tend to be shifted toward the low-frequency part of the spectrum due to the significant attenuation of the basalt layers. Figure 11 illustrates the results of the velocity analysis by applying the C_{cm} functional with different wavelet spectra. The application of matching wavelets with central frequency from 5 to 20 Hz at steps of 5 Hz is shown in Figure 11a–11d, respectively. Note that coherency maxima pertinent to subbasalt reflections do appear in the velocity spectra when matching filters are centered on 5 and 10 Hz (Figure 11a and 11b), whereas higher frequencies (15 and 20 Hz) tend to obliterate these events in the velocity panels (Figure 11c and 11d).

CONCLUSIONS

High-resolution coherency measures such as those based on the covariance of the data along hyperbolic trajectories and on the complex matched analysis are able to detect weak reflections in noise-contaminated data and resolve interference among primaries and multiples. From a practical point of view, the C_{cm} and C_{cmKS} coherency functionals give similar results, though the C_{cmKS} has a higher resolution, especially along the velocity axis. However, C_{cmKS} requires a higher computational time. The computing cost of the C_{cm} and the C_{cmKS} functionals is 2.5 and 4.4 times the cost of the semblance coefficient, respectively. We believe that high-resolution functionals could be exploited in subbasalt exploration, where it is common to face the problem of detecting subbasalt reflections that are generally at a very low amplitude, have high levels of noise contamination, and are interfered with by multiples. To test the effectiveness of the proposed high-resolution velocity analysis, we made use of synthetic and field data, and the outcomes were satisfactory. In both cases, the high-resolution coherency functionals performed better than the standard semblance analysis and were able to spot the weak subbasalt primary reflections in a situation of very low S/N and strong multiple contamination. This performance is enhanced by the possibility of using different matching wavelets that better fit the target signals.

In the present implementation of our codes, the wavelet and the sliding time window for velocity analysis are fixed. Therefore, in the search for low-frequency subbasalt signals, the wavelet central frequency and the width of the time window must be set at a low frequency and at a large enough time width, respectively. Obviously, this setting is not optimal for the analysis of shallower reflections characterized by shorter pulses, which in any case do not represent a problem because they are quite evident in any coherency panel.

Accurate knowledge of the subbasalt stacking velocities makes it possible to perform more efficient and accurate operations aimed either at primary signal enhancement or at multiple removal.

We applied very limited preprocessing to our field data examples to maintain the data as much as possible in their pristine condition to avoid the risk of introducing artifacts or altering possible weak signals from the subbasalt layers. In fact, in a separate study, we verify that the application of various denoising and demultiple operations, although attenuating noise and removing multiples, may also severely damage the primary signal. Therefore, it is advisable to first identify the subbasalt primaries (if detectable) and the various multiples or other events (such as converted waves or other kinds of coherent noise). We propose using the velocity analysis with the high-resolution functionals previously described. Then, once we have discerned the primary signal from the other events in terms of distinct coherency maxima, we can use this information to drive the subsequent signal enhancement and denoising operations. In addition, the high-resolution coherency functionals we have discussed in relation to stacking velocity analysis can also be applied to focusing analysis of common image gathers following prestack depth migration.

REFERENCES

Abbad, B., and B. Ursin, 2012, High-resolution bootstrapped differential semblance: Geophysics, **77**, no. 3, U39–U47, doi: 10.1190/geo2011-0231.1.

Abbad, B., B. Ursin, and D. Rappin, 2009, Automatic nonhyperbolic velocity analysis: Geophysics, **74**, no. 2, U1–U12, doi: 10.1190/1.3075144.

Biondi, B. L., and C. Kostov, 1989, High-resolution velocity spectra using eigenstructure methods: Geophysics, **54**, 832–842, doi: 10.1190/1.1442712.

Fliedner, M. M., and R. S. White, 2001, Seismic structure of basalt flows from surface seismic data, borehole measurements, and synthetic seismogram modeling: Geophysics, **66**, 1925–1936, doi: 10.1190/1.1486760.

Fruehn, J., M. M. Fliedner, and R. S. White, 2001, Integrated wide-angle and near-vertical subbasalt study using large-aperture seismic data from the Faeroe-Schetland region: Geophysics, **66**, 1340–1348, doi: 10.1190/1.1487079.

Gallagher, J., and P. Dromgoole, 2008, Seeing below the basalt — Offshore Faroes: Geophysical Prospecting, **56**, 33–45, doi: 10.1111/j.1365-2478.2007.00670.x.

Grandi, A., A. Mazzotti, and E. Stucchi, 2007, Multicomponent velocity analysis with quaternions: Geophysical Prospecting, **55**, 761–777, doi: 10.1111/j.1365-2478.2007.00657.x.

Grandi, A., E. Stucchi, and A. Mazzotti, 2004, Multicomponent velocity analysis by means of covariance measures and complex matched filters: 74th Annual International Meeting, SEG, Expanded Abstracts, 2415–2418.

Grion, S., A. Mazzotti, and U. Spagnolini, 1998, Joint estimation of AVO and kinematics parameters: Geophysical Prospecting, **46**, 405–422, doi: 10.1046/j.1365-2478.1998.970332.x.

Jones, I. F., and S. Levy, 1987, Signal-to-noise ratio enhancement in multi-channel seismic data via the Karhunen-Loève transform: Geophysical Prospecting, **35**, 12–32, doi: 10.1111/j.1365-2478.1987.tb00800.x.

Key, S. C., L. Kirlin, and S. B. Smithson, 1987, Seismic velocity analysis using maximum-likelihood weighted eigenvalue ratios: 57th Annual International Meeting, SEG, Expanded Abstracts, 461–464.

Key, S. C., and S. B. Smithson, 1990, New approach to seismic-reflection event detection and velocity determination: Geophysics, **55**, 1057–1069, doi: 10.1190/1.1442918.

Neidell, N. S., and M. T. Taner, 1971, Semblance and other coherency measures for multichannel data: Geophysics, **36**, 482–497, doi: 10.1190/1.1440186.

Sacchi, M. D., 1998, A bootstrap procedure for high-resolution velocity analysis: Geophysics, **63**, 1716–1725, doi: 10.1190/1.1444467.

Sguazzero, P., and A. Vesnaver, 1987, A comparative analysis of algorithms for seismic velocity estimation, *in* M. Bernabini, F. Rocca, S. Treitel, and M. Worthington, eds., Deconvolution and inversion: Blackwell Scientific Publications Inc., 267–286.

Spagnolini, U., L. Maciotta, and A. Manni, 1993, Velocity analysis by truncated singular value decomposition: 63rd Annual International Meeting, SEG, Expanded Abstracts, 677–680.

Spitzer, R., R. S. White, and P. A. F. Christie, 2003, Enhancing subbasalt reflections using parabolic τ-p transformation: The Leading Edge, **22**, 1184–1201, doi: 10.1190/1.1641371.

Spjuth, C., P. B. Sabel, S. K. Foss, P. Dromgoole, C. Friedrich, J. Herredsvela, A. Day, P. E. Dhelie, S. Hegna, T. Hly, and K. Koch, 2012, Broadband seismic for subbasalt exploration: 74th Annual International Conference and Exhibition, EAGE, Extended Abstracts, B036.

White, R. S., J. R. Smallwood, M. M. Fliedner, B. Boslaugh, J. Maresh, and J. Fruehn, 2003, Imaging and regional distribution of basalt flows in the Faeroe-Shetland Basin: Geophysical Prospecting, **51**, 215–231, doi: 10.1046/j.1365-2478.2003.00364.x.

Woodburn, N., A. Hardwick, and T. Travis, 2011, Enhanced low frequency signal processing for sub-basalt imaging: 81st Annual International Meeting, SEG, Expanded Abstracts, 3673–3677.

Zhou, Z. Z., M. Cvetkovic, B. Xu, and P. Fontana, 2012, Analysis of a broadband processing technology applicable to conventional streamer data: First Break, **30**, 77–82.

Ziolkowski, A., P. Hanssen, R. Gatliff, H. Jakubowicz, A. Dobson, G. Hampson, X. Li, and E. Liu, 2003, Use of low frequencies for sub-basalt imaging: Geophysical Prospecting, **51**, 169–182, doi: 10.1046/j.1365-2478.2003.00363.x.